ELECTROCHEMISTRY

Identifying the positive role of lithium hydride in stabilizing Li metal anodes

Hongyu Zhang, Shunlong Ju, Guanglin Xia*, Xuebin Yu*

Lithium hydride has been widely identified as the major component of the solid-electrolyte interphase of Li metal batteries (LMBs), but is often regarded as being detrimental to the stabilization of LMBs. Here, we identify the positive and important role of LiH in promoting fast diffusion of Li ions by building a unique three-dimensional (3D) Li metal anode composed of LiMg alloys uniformly confined into graphene-supported LiH nanoparticles. The built-in electric field at the interface between LiH with high Li ion conductivity and LiMg alloys effectively boosts Li diffusion kinetics toward favorable Li plating into lithiophilic LiMg alloys through the surface of LiH. Therefore, the diffusion coefficient of Li ions of the thus-formed 3D structured Li metal anode is 10 times higher than the identical anode without the presence of LiH, and it exhibits a long cycle life of over 1200 hours at 3 mA cm^{-2} under 5 mA hour cm^{-2}.

INTRODUCTION

The ever-increasing demand for advanced electric vehicles and portable electronic devices has raised great interest in developing high–energy density lithium-ion batteries (LIBs) (1–3). Replacing the applied graphite anode in current LIBs with metallic Li, which has an ultrahigh specific capacity of 3860 mA hour g^{-1} and the lowest reduction potential (−3.04 V versus standard hydrogen electrodes), has long been considered as an effective strategy to increase the energy density of current LIBs to be over 300 watt-hour (Wh) kg^{-1} (4–6). The practical application of lithium metal batteries (LMBs), however, is still hindered by the uneven deposition of Li that results in uncontrollable growth of dendritic Li, which could cause short life and safety risks due to the possible pierce of the separator (7, 8). Moreover, the infinite volume change during the Li stripping/plating process is capable of breaking the originally fragile solid electrolyte interface (SEI) formed by the thermodynamically favorable reaction between Li and electrolyte, leading to the accelerated growth of Li dendrites. The continuous formation of Li dendrites leads to the dry-up of the electrolyte with low coulombic efficiency, the accumulation of "dead Li," and, eventually, the failure of batteries (9, 10).

Considering the important role of SEI in tuning the Li stripping and plating behavior of Li metal anodes, the determination of the components of SEI has been the focus of the research for developing stable Li metal anodes. Recently, it has been widely demonstrated that lithium hydride is one of the major components of SEI layers with high abundance (11–14). However, the continuous formation of LiH, on one hand, could undoubtedly contribute to the severe loss of capacity and is capable of forming dendrites composed of LiH instead of Li metal, eventually causing safety concerns. Moreover, because of its poor electrical conductivity and brittle nature, the formation of LiH has been regarded as the main reason to induce the pulverization process of Li metal anode during cycling Li stripping and plating behavior. Therefore, it is generally accepted that the formation of LiH plays a negative role in developing dendrite-free Li metal anode.

Here, we demonstrate the positive role of LiH in suppressing the growth of Li dendrites by building a three-dimensional (3D) Li metal anode composed of solid-solution LiMg alloys uniformly confined into graphene-supported LiH nanoparticles (denoted as LiMg-LiH@G) via the roll-press method of Li metal and graphene-supported MgH$_2$ nanoparticles (denoted as MgH$_2$@G). The favorable reaction between MgH$_2$ nanoparticles uniformly distributed on graphene and Li metal results in the homogeneous formation of solid-solution LiMg alloys across the whole scaffold with uniformly distributed LiH and graphene. The lithiophilic LiMg alloys with high solubility of Li could first act as homogeneous nucleation sites and improve the Li stripping and plating process based on the reversible solid solution–based alloying reaction. Theoretical and experimental observation confirms that the uniform building of the interface between LiH and LiMg alloys results in the formation of numerous built-in electric fields at the interface between LiH and LiMg alloys, which effectively promotes Li ion transport from the surface of LiH with high Li ion conductivity to the surface of LiMg alloys toward favorable Li plating into LiMg alloys. Therefore, the diffusion coefficient of Li ions of LiMg alloys confined into graphene-supported LiH nanoparticles is 10 times higher than that of pure LiMg alloys confined into graphene, boosting fast Li ion transportation across the whole electrode. In addition, the conductive 3D frameworks built by the uniformly distributed graphene not only alleviate the large volume change during the Li stripping/plating process but also reduce local current density, leading to the suppressed formation of dendritic Li and improved the cycling stability of Li metal anodes. As a result, the as-fabricated LiMg-LiH@G with a high specific capacity of 3252 mA hour g^{-1}, which is higher than most of the reported 3D structured Li metal anodes (15–19), exhibits a long cycle life of over 1200 hours at a high current density of 3 mA cm^{-2} with a fixed capacity of 5 mA hour cm^{-2}. More impressively, upon coupling ultrathin LiMg-LiH@G foil (50 μm, ~8.4 mA hour cm^{-2}) as the anode with commercial LiFePO$_4$ (LFP; 12 mg cm^{-2}) and LiNi$_{0.5}$Co$_{0.2}$Mn$_{0.3}$O$_2$ (NCM523; 10 mg cm^{-2}) cathode, the assembled full cells show remarkable cycling stability of over 200 cycles at 1 C.

RESULTS

Graphene-supported uniform MgH$_2$ nanoparticles were synthesized through solvothermal reaction of dibutyl magnesium under the structure-directing of graphene (fig. S1) (20). The loading amount of MgH$_2$ on graphene is calculated to be about 63% based on the

Department of Materials Science, Fudan University, Shanghai 200433, China.
*Corresponding author. Email: xiaguanglin@fudan.edu.cn (G.X.); yuxuebin@fudan.edu.cn (X.Y.)

hydrogen desorption capacity of MgH$_2$@G, according to the thermogravimetric results (fig. S2). Scanning electron microscopy (SEM) and transmission electron microscopy (TEM) images (fig. S3) demonstrate that the as-synthesized MgH$_2$ nanoparticles with an average particle size of 8 nm are distributed homogeneously on graphene (MgH$_2$@G). The porous structure constructed by graphene layers provides sufficient room for the infiltration of molten Li and hence could effectively promote the chemical reaction between MgH$_2$ and molten Li. As schematically illustrated in Fig. 1A, the 3D structured LiMg-LiH@G anode is fabricated by mixing a certain amount of MgH$_2$@G [5, 9, 13, and 17 weight % (wt %)] with Li foil by rolling and pressing for several times, followed by thermal heating. X-ray diffraction (XRD) patterns confirm the formation of LiMg alloys and LiH in the as-obtained LiMg-LiH@G electrode (Fig. 1B), which agrees well with the observation of LiMg alloys at 1302.5 eV and LiH at 55.5 eV in the x-ray photoelectron spectroscopy (XPS) results (Fig. 1, C and D). The as-formed LiMg alloys exhibit a typical body-centered cubic crystal structure, indicating the formation of solid-solution LiMg alloys with homogeneous distribution of Mg in Li matrix (fig. S4). Induced by the favorable interaction between MgH$_2$ nanoparticles and Li, uniform distribution of LiH and graphene inside the as-formed LiMg alloys could be achieved. Therefore, the as-prepared LiMg-LiH@G foil exhibits a smooth surface after thermal heating (Fig. 1, E and F). The corresponding elemental mapping

results illustrate that Mg and C are evenly distributed across the whole electrode, which proves that LiMg alloys and graphene-supported LiH nanoparticles are uniformly dispersed inside the LiMg-LiH@G anode owing to the favorable reaction between MgH$_2$@G and Li induced by uniformly distributed MgH$_2$ nanoparticles and the porous structure of layered and winkled graphene of pristine MgH$_2$@G. After stripping away Li metal, the color of the LiMg-LiH@G foil turns from silver back to black (fig. S5) and the 3D structure composed of uniformly dispersed graphene sheets and Li-poor LiMg/LiH nanoparticles is well maintained (fig. S6), which provides additional evidence to the uniform construction of 3D structured anode by confining solid-solution LiMg alloys into graphene-supported LiH nanoparticles.

To evaluate the cycling performance and reversibility of LiMg-LiH@G with various amounts of MgH$_2$@G, symmetric cells are first fabricated and tested at 1 mA cm^{-2} with an areal capacity of 1 mA hour cm^{-2} (fig. S7). In the case of the bare Li anode, the overpotential increases rapidly after only 250 hours, and reaches 100 mV after 400 hours, indicating the accumulation of "dead Li" originating from the peel-off of Li dendrites due to the large volume change upon cycling, which impedes the fast diffusion of Li ions. In strong contrast, the as-prepared LiMg-LiH@G anodes with various amounts of MgH$_2$@G exhibit much better cycling stability with lower overpotential, indicating that the building of lithiophilic solid-solution LiMg alloys confined into LiH@graphene scaffolds could effectively
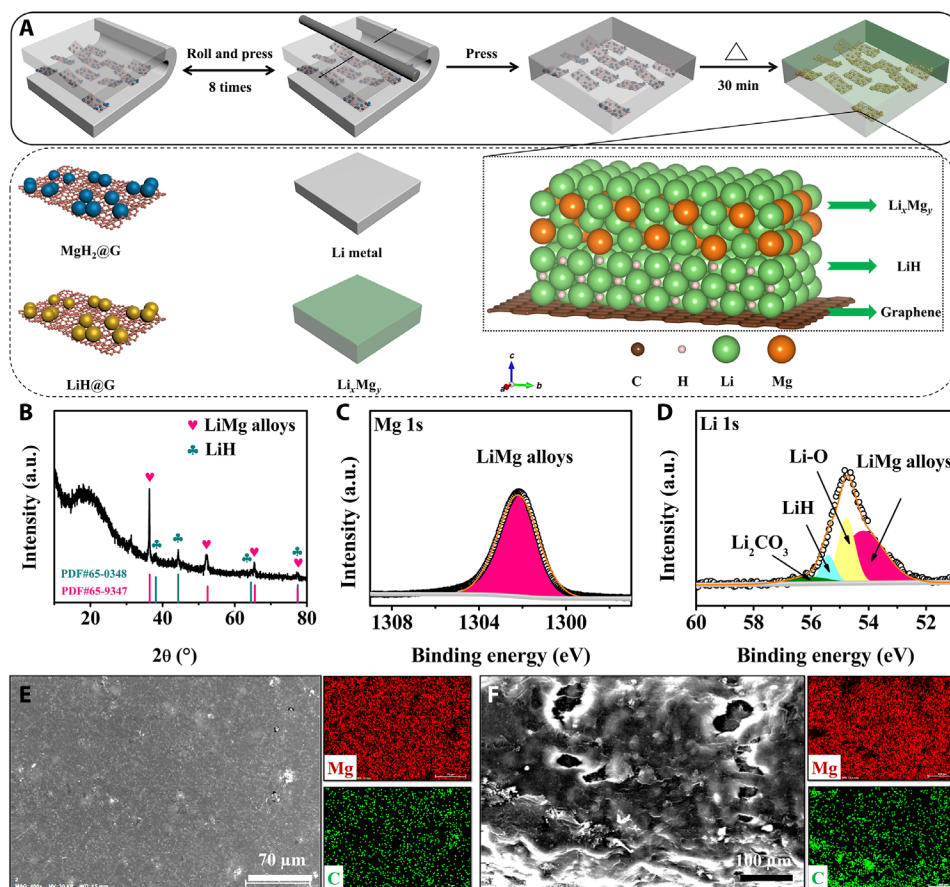

Fig. 1. Fabrication strategy and the characterization of the LiMg-LiH@G electrode. (**A**) Schematic illustration of the fabrication of the LiMg-LiH@G electrode. (**B**) XRD pattern, high-resolution Mg 1s (**C**) and Li 1s (**D**) XPS spectra after Ar ion etching for 50 nm, and top-view (**E**) and cross-sectional (**F**) SEM images, as well as the corresponding elemental mapping, of the LiMg-LiH@G electrode. a.u., arbitrary units.

alleviate the formation of Li dendrites and dead Li and hence improve the reversibility of Li stripping/plating process. Among them, the LiMg-LiH@G electrode fabricated with 9 wt % MgH$_2$@G exhibits the best performance with a stable cycle life of over 1700 hours and a low overpotential of only ~16 mV after cycling, which is adopted for further investigation in detail. Upon using Mg@G to stabilize Li metal anode (denoted as LiMg-G), a notable improvement of cycling performance could also be observed for the thus-formed LiMg-G anode compared with the bare Li metal anode, indicating that the graphene-confined lithiophilic LiMg alloys with high solubility of Li (fig. S8), serving as homogeneous nucleation sites, improves both the Li stripping and plating process based on the reversible solid solution–based alloying reaction (21) and the cycling stability due to the alleviated volume change induced by the space-confinement role of graphene (22–24). The cycling stability of LiMg-G with certain content of Mg@G, however, is far inferior to LiMg-LiH@G with the same amount of MgH$_2$@G, respectively (fig. S9). This result directly demonstrates that in addition to the role of graphene with interconnected lithiophilic LiMg alloys, the uniform introduction of LiH in the electrode plays an important role in further improving the cycling reversibility of Li stripping and plating process.

To deeply understand the effect of LiH in enhancing the stability of LiMg-LiH@G, theoretical calculations by using density functional theory (DFT) are subsequently conducted. The introduction of MgH$_2$ into Li metal anode inevitably generates numerous interfaces of LiH/LiMg alloys across the entire electrode, which would play an important role in the adsorption and diffusion behavior of Li inside the anode. Therefore, models, which stand for the interfaces of LiMg alloys/LiMg alloys and LiH/LiMg alloys, are first constructed in this work, and Li$_3$Mg is chosen to represent Li-rich LiMg alloys in the LiMg-G and LiMg-LiH@G anode. It is worth noting that although the lihiophilic LiMg alloys promotes uniform Li nucleation and regulates Li plating process, the diffusion barrier at the interface of Li$_3$Mg (001)/Li$_3$Mg (001) reaches 0.49 eV (Fig. 2, A and B), corresponding well with the high diffusion barrier of Li ions on the surface of Li$_3$Mg alloys (21), which retards the diffusion and uniform plating of Li inside the electrode. By comparison, upon the introduction of LiH with a much lower Li ion diffusion barrier than that of LiMg alloys (21), the diffusion barrier at the interface of LiH (001)/Li$_3$Mg (001) is significantly decreased to 0.38 eV (Fig. 2, C and D). It directly demonstrates that the homogeneous introduction of LiH into LiMg alloys could effectively enhance the Li diffusion kinetics inside the LiMg-LiH@G electrode. Charge analysis results demonstrate that owing to the poor electronegativity of H in the ionic compound of LiH, the charge on LiH could be easily freed and transferred, resulting in the charge accumulation at the interface of Li$_3$Mg and the charge depletion regions at the interface of LiH as evidenced by the charge density difference map, which could be well preserved upon the diffusion of Li ions (fig. S10). This result directly confirms the charge transfer from LiH to Li$_3$Mg, leading to the establishment of a built-in electric field directed from Li$_3$Mg to LiH, which therefore facilitates fast diffusion kinetics of Li ion transferred through the surface of LiH to the surface of LiMg alloys toward favorable Li plating into LiMg alloys. Therefore, the fast diffusion pathway of Li ions across the whole electrode could be built based on the synergistic role of LiH/LiMg interfaces in promoting Li ion diffusion by virtue of the surface of LiH and facilitating Li ions transfer to the surface of LiMg alloys toward favorable Li deposition.

Although LiH is calculated to be lithiophobic (21), the binding energy of Li atom at the interface of LiH (001)/Li$_3$Mg (001) is still as low as −2.6 eV, comparable to that of Li$_3$Mg (001)/Li$_3$Mg (001) (i.e., −2.69 eV), which is much lower than that of Li metal (−2.26 eV) (fig. S11). These results validate that the introduction of LiH is able to improve the Li diffusion across the whole electrode without sacrificing the lithiophilicity of LiMg alloys and hence improve the stability of Li stripping and plating of the electrode. Therefore, Li would prefer to deposit at the interface of both LiH/LiMg alloys and LiMg/LiMg alloys. As a result, owing to the solid solution–based alloying process of LiMg alloys that leads to facile Li diffusion inside LiMg alloys and the uniform distribution of numerous interfaces of LiH/LiMg alloys (25, 26), Li would inevitably go through the interface of LiH/LiMg alloys upon initial Li deposition at the interface of LiH/LiMg alloys and/or LiMg/LiMg alloys. Hence, the synergistic role of LiH/LiMg interfaces in promoting Li ion diffusion and facilitating Li ions transfer to the surface of LiMg alloys toward favorable Li deposition would effectively improve the Li diffusion kinetics during Li deposition into LiMg-LiH@G. In addition, upon cycling, although LiMg-LiH@G with poor distribution of LiH and graphene (denoted as LiMg-LiH@G-2) shows better performance than bare Li, its cycling stability is much inferior to that of LiMg-LiH@G with uniform distribution of LiH and graphene (fig. S12). This finding reveals that the uneven dispersion of LiH@G inside LiMg-LiH@G would result in inhomogeneous Li deposition and poor cycling stability due to the heterogeneous Li diffusion rate at different locations inside LiMg alloys, which provides indirect evidence to the indispensable effect of LiH in boosting Li diffusion inside LiMg alloys. To further confirm the fast diffusion of Li achieved by building the interface of LiH/LiMg alloys, the diffusion of Li$^+$ in the electrode is subsequently measured during the lithiation of LiMg-LiH@G and LiMg-G after complete delithiation by galvanostatic intermittent titration technique (GITT) (Fig. 2E). The diffusion coefficient of Li$^+$ (D_{Li}) of MgH$_2$@G after complete lithiation is calculated to be around 1.49×10^{-8} cm^2 s^{-1}, much higher than that of Mg@G (2.05×10^{-9} cm^2 s^{-1}), and the D_{Li} of both MgH$_2$@G and Mg@G is orders of magnitude higher than the self-diffusion coefficient of Li metal (10^{-11} cm^2 s^{-1}) (27). This demonstrates that the introduction of both LiMg alloys and LiH could promote the diffusion of Li ions inside the LiMg-LiH@G electrode. Therefore, the as-formed LiH-graphene framework in LiMg-LiH@G could not only reduce the local current density and accommodate the volume change during cycling but also provide an ion/electron conductive network across the whole electrode, synergistically enhancing the cycling reversibility of the electrode.

The electrochemical Li plating/stripping behavior of LiMg-LiH@G anodes, in comparison with LiMg-G and bare Li, is further investigated under high current densities. When the applied current density is increased to 3 mA cm^{-2} (Fig. 2F), the overpotential of the bare Li anode increases to be over 200 mV after only 300 hours due to the severe dendrite formation at high current densities, while a prolonged life span of 350 hours could be observed for the LiMg-G electrode due to the formation of lithiophilic LiMg alloys. In strong contrast, an ultralong cycle life of 800 hours with a low overpotential of only 20 mV is achieved for LiMg-LiH@G. Moreover, LiMg-LiH@G exhibits superior rate capability than both LiMg-G and bare Li metal (Fig. 2G). Stable cycling performance with a small overpotential value of 11, 23, 42, and 68 mV is observed for LiMg-LiH@G at 1, 3, 5, and 8 mA cm^{-2}, respectively. It is reported that upon the increase of
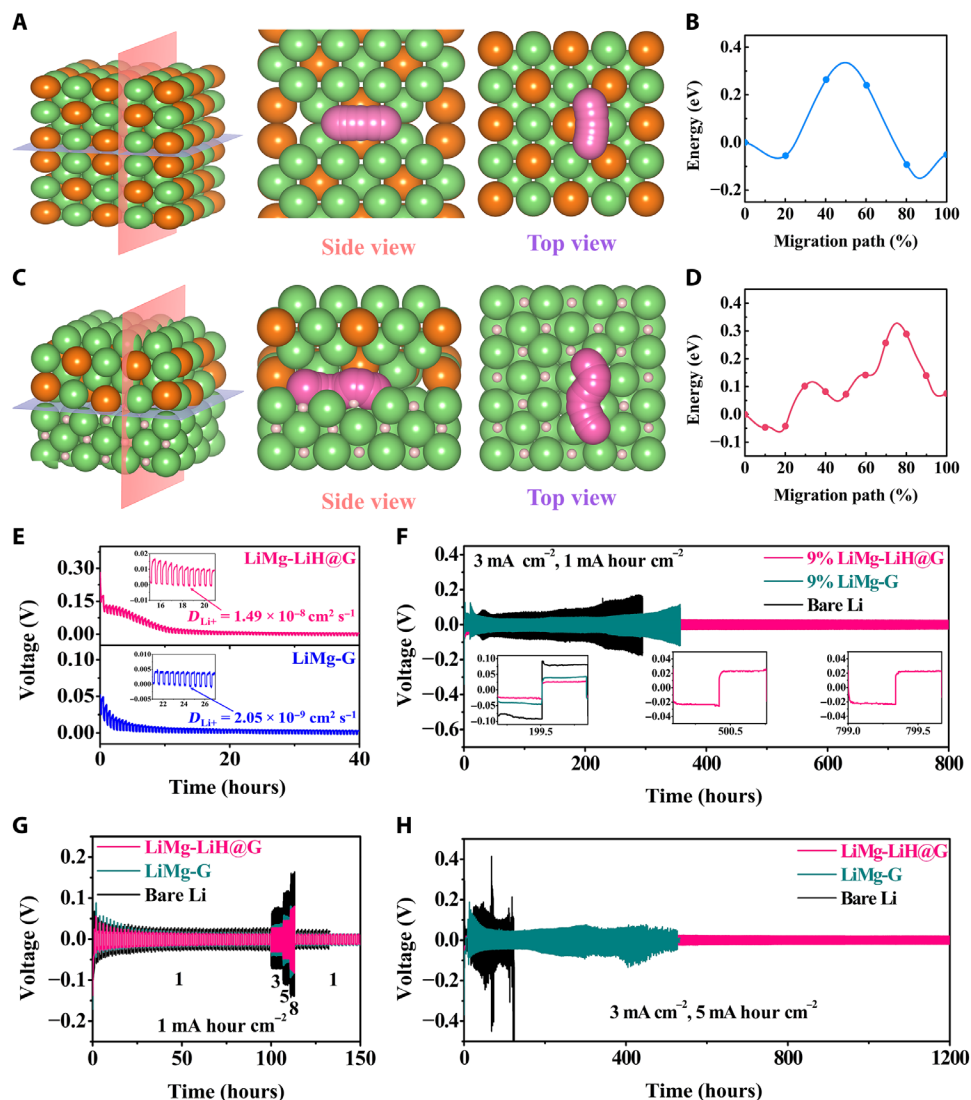
Fig. 2. DFT calculations and electrochemical performance of various anodes in half and symmetric cells. (**A** and **C**) The diffusion pathway and (**B** and **D**) calculated energy profile of Li along the diffusion path at the interface of Li_3Mg_7 (001)/Li_3Mg_7 (001) and LiH (001)/Li_3Mg_7 (001), respectively. The orange, green, and pink balls denote Mg, Li, and adsorbed Li atoms, respectively. (**E**) GITT curves during the lithiation of LiMg-LiH@G and LiMg-G after complete delithiation for calculating the corresponding Li ion diffusion coefficient. (**F**) Galvanostatic discharge/charge voltage profiles of 9% LiMg-LiH@G, 9% LiMg-G, and bare Li electrode in symmetric cells at 3 mA cm^{-2} with a fixed areal capacity of 1 mA hour cm^{-2}. (**G**) Rate performance of LiMg-LiH@G and bare Li electrode in symmetric cells at various current densities. (**H**) Galvanostatic discharge/charge voltage profiles of the LiMg-LiH@G electrode with 9% MgH_2@G and bare Li electrode in symmetric cells at 3 mA cm^{-2} with a fixed areal capacity of 5 mA hour cm^{-2}.

areal capacity, the large volume change of Li metal anode will aggravate the fracture and reformation of SEI layers, the growth of dendritic Li, and the formation of dead Li, leading to the severe degradation of cycling stability (*10*, *28*). Therefore, the bare Li anode shows large voltage fluctuation and high voltage hysteresis of over 800 mV after only 120 hours at 3 mA cm^{-2} with a high areal capacity of 5 mA hour cm^{-2} (Fig. 2H). Although this phenomenon could be alleviated for the LiMg-G electrode to some extent, short circuit could still be observed after 540 hours. By comparison, LiMg-LiH@G exhibits long-term cycling stability of over 1200 hours with a low overpotential of 22 mV under identical conditions, which demonstrates the capability of the 3D LiMg-LiH@G electrode in suppressing the formation of Li dendrites even at high current densities with

high areal capacities. These results verify that the 3D network of LiH-graphene could not only reduce the local current density to postpone the formation of Li dendrites but also accommodate the large volume change even at high current densities with high areal capacities, thus leading to stable cycling performance. The uniform formation of lithiophilic LiMg alloys could effectively improve the cycling stability of LiMg-G, and the introduction of LiH, which could promote the diffusion of Li ion inside LiMg alloys, could further prolong the life span of LiMg-LiH@G. Electrochemical impedance spectroscopy (EIS) measurements are subsequently adopted to investigate the interfacial charge transfer in symmetric cells upon cycling (fig. S13 and table S2). A comparable interfacial charge transfer resistance (R_{ct}) could be observed for LiMg-LiH@G and the bare Li

anode after first cycle. Upon cycling before 50 cycles, the R_{ct} of both LiMg-LiH@G and bare Li decreases due to the rupture of the native SEI layer that is naturally formed on the surface of Li metal resulting from its high reactivity and the formation of high-surface-area Li dendrites, which leads to the increase of the surface area of Li metal and hence the decrease of charge transfer resistance (fig. S14) (29). After 100 cycles, the R_{ct} of the bare Li anode increases to 32 ohms due to the continuous accumulation of dead Li and the formation of serious cracks on the surface of Li metal, while only negligible change of R_{ct} could be observed for the LiMg-LiH@G anode, indicating a stable structural integrity of the LiMg-LiH@G electrode, which could effectively suppress the formation of Li dendrites and dead Li. It is noteworthy that although a lower R_{ct} of 19.6 ohms could be observed for LiMg-G compared with the bare Li anode due to the positive role of graphene and LiMg alloys in enhancing the stability of Li plating and stripping process, this value is still much higher than that of LiMg-LiH@G after 100 cycles, which provides additional evidence to the indispensable effect of LiH in improving the diffusion of Li$^+$ across the electrode. Moreover, the exchange current density (I_0) of LiMg-LiH@G (6.76 mA cm^{-2}) is also much higher than that of both LiMg-G (4.63 mA cm^{-2}) and the bare Li anode (2.37 mA cm^{-2}) after cycling (fig. S15). During the Li stripping and plating process, the I_0 of LiMg-LiH@G could be well preserved after 50 cycles, which is still much higher than that of both LiMg-G (3.97 mA cm^{-2}) and the bare Li anode (2.75 mA cm^{-2}) (fig. S16). These results further verify that the uniformly distributed LiH in the LiMg-LiH@G electrode could enhance the interfacial transport of Li ions. In addition, the symmetric cells are also tested in commercial carbonate electrolyte, in which the LiMg-LiH@G electrode exhibits stable cycling for 1600 and 500 hours with a low overpotential of 40 and 70 mV at 1 mA cm^{-2} (fig. S17) and 2 mA cm^{-2} (fig. S18), respectively, with a fixed capacity of 1 mA hour cm^{-2}. A cycle life of over 500 h at 2 mA cm^{-2} with a fixed capacity of 3 mA hour cm^{-2} could be obtained for the LiMg-LiH@G electrode (fig. S19), which is among the best reported Li metal anodes so far (table S1).

The morphology analysis is subsequently conducted to gain insights into the enhanced electrochemical performance of LiMg-LiH@G. After stripping 2 mA hour cm^{-2} of Li at 1 mA cm^{-2}, the surface of bare Li is already full of pits, demonstrating the uneven Li stripping process (Fig. 3A), which could induce severe uneven Li deposition upon replating 2 mA hour cm^{-2} of Li (Fig. 3B). When the stripping capacity is increased to 5 mA hour cm^{-2}, the nonuniform pits become more apparent and deeper (fig. S20A). As a result, a long tubular and moss-like Li structure could be observed on the surface of bare Li after the reversible Li replating process (fig. S20B). After 100 cycles, a porous dead Li layer with many cracks is accumulated on the surface of bare Li (fig. S21), which would impede the diffusion of Li$^+$ and hence result in large polarization after a few cycles. In strong contrast, LiMg-LiH@G exhibits a dendrite-free and smooth surface under an applied capacity of 2 mA hour cm^{-2} (Fig. 3, C and D), and it could be well preserved upon increasing the applied capacity to 5 mA hour cm^{-2} (fig. S20, C and D) owing to the fast Li$^+$ transfer inside the LiMg-LiH@G electrode. A uniform surface with a dense activated LiMg layer could still be observed for the LiMg-LiH@G electrode after 100 cycles due to the dense and uniform dissolution/deposition of Li (Fig. 3E). The elemental mapping of the cycled LiMg-LiH@G electrode further demonstrates the uniform distribution of Mg and C in the whole matrix (fig. S22),

indicating the stable structural integrity of the LiMg-LiH@G electrode with a good distribution of LiMg alloys and the LiH-graphene network, which could effectively suppress the formation of dendritic or moss-like Li metal and hence improve the cycling stability of LiMg-LiH@G.

The chemical environment of Li metal anode upon cycling is further investigated by depth profiling of XPS via Ar ion etching (fig. S23) and LiMg-LiH@G (Fig. 3F) after 20 cycles. The N 1s peaks at 398.3 eV, as well as the Li 1s peak at 54.6 eV, could be attributed to Li$_3$N (30, 31), originating from the decomposition of lithium bis(trifluoromethane)sulfonimide (LiTFSI) and LiNO$_3$. In parallel, the peak at 685.3 eV in the F 1s spectrum and the peak at 56.2 eV in the Li 1s spectrum could be attributed to the formation of LiF due to the break of the C-F bond in LiTFSI. Before Ar ion etching, the surface of both bare Li and LiMg-LiH@G is mainly composed of LiF, LiH, Li-O-, and Li$_3$N, which are common components of SEI layers formed in ether-based electrolyte, whereas the LiMg alloys at 1302.7 eV and some species of Mg-containing compounds at 1303.2 eV in the Mg 1s spectrum could be observed on the surface of the LiMg-LiH@G electrode. With the increase of etching depth, only negligible change of the peak intensity of LiF, LiH, Li-O, and Li$_3$N could be observed for the bare Li metal anode, indicating that the thickness of SEI layers on bare Li is much higher than 400 nm, resulting from the continuous formation of SEI layers due to the large volume change during the Li stripping/deposition process. In contrast, the peak intensity of SEI components, except for LiH, of LiMg-LiH@G decreases rapidly upon the increase of etching depth, suggesting the formation of SEI layers with a smaller thickness compared with that of the bare Li metal anode. Moreover, the characteristic peak of LiMg alloys in the Li 1s spectrum becomes dominated with the increase of etching time, which provides further evidence for the formation of much thinner SEI layers on the LiMg-LiH@G electrode. The amount of LiH of LiMg-LiH@G remains stable after cycling, while obvious formation of LiH could be observed for the bare Li metal anode, indicating the suppressed formation of LiH in SEI upon repeated Li stripping and plating process (fig. S24). These results further demonstrate that the building of the 3D structured LiMg-LiH@G electrode could not only induce dense and uniform stripping and plating of Li but also effectively alleviate the side reaction between Li and electrolyte toward enhanced cycling stability.

To evaluate the potential practical applications of LiMg-LiH@G, full cells coupled with commercial cathodes are assembled and tested. The specific capacity of LiMg-LiH@G is first evaluated by galvanostatic charging to confirm the N/P ratio in full cell test (Fig. 4A), which shows a high specific capacity of 3252 mA hour g^{-1} for LiMg-LiH@G (activated Li in LiMg-LiH@G, 84.2 wt %), comparable to the theoretical specific capacity of Li. First, LFP with a mass loading of 12 mg cm^{-2} (~2 mA hour cm^{-2}) is used as the cathode, and ultrathin LiMg-LiH@G and Li foil (~50 μm) are used as the anode to reach a practically low anode/cathode ratio of 4.2:1 and 5:1, respectively. Although LiMg-LiH@G//LFP exhibits a similar capacity to bare Li//LFP at low rates (i.e., ~1.92 mA hour cm^{-2} at 0.5 C and ~1.81 mA hour cm^{-2} at 1 C) in rate performance tests (Fig. 4B and fig. S25), a higher areal capacity at high rate (i.e., 1.69 mA hour cm^{-2} and 1.46 mA hour cm^{-2} at 2 and 4 C, respectively) could be achieved for LiMg-LiH@G//LFP full cells. Moreover, when the current density is changed back to 1 C, the reversible capacity of LiMg-LiH@G//LFP could be fully recovered, indicating stable reversibility of the
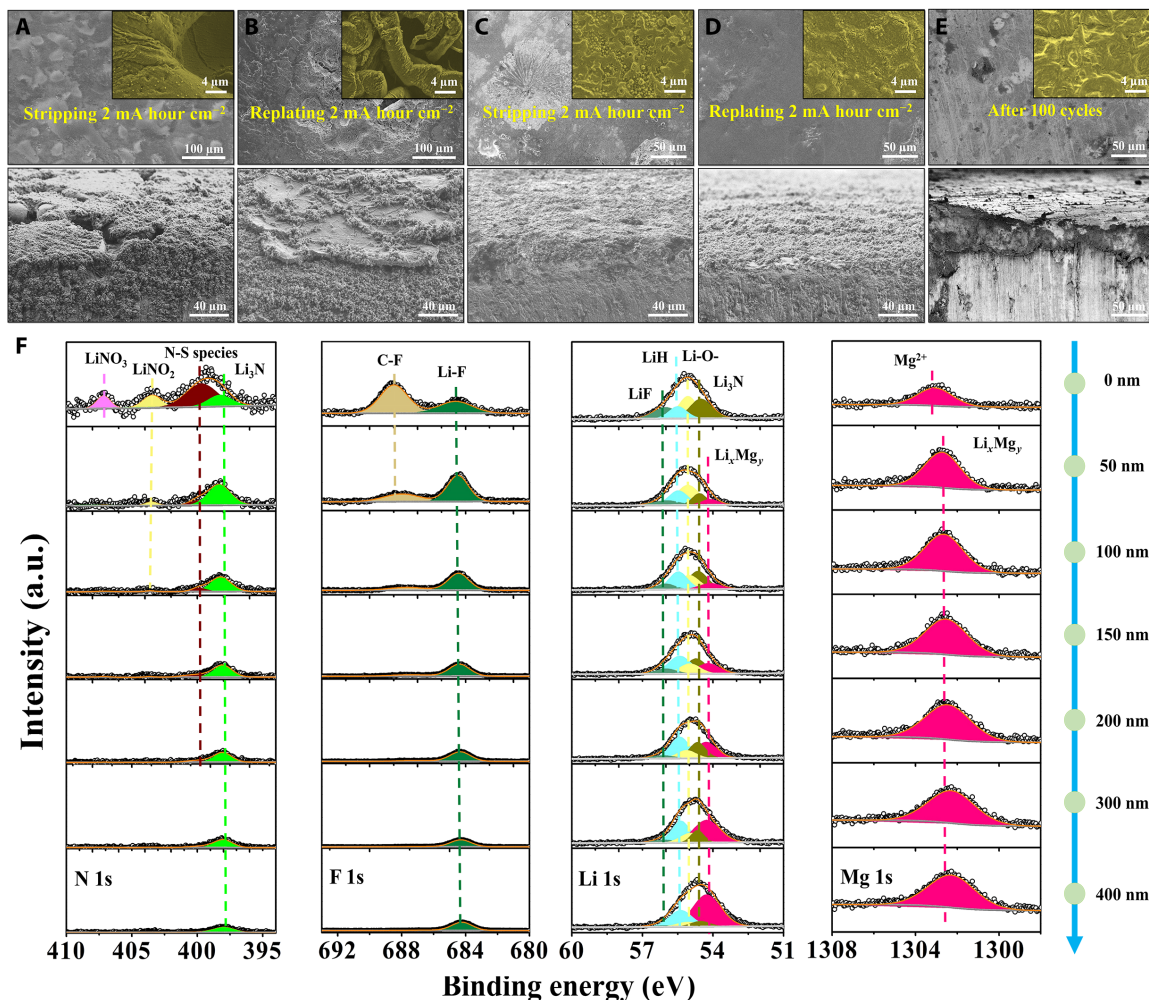
Fig. 3. Morphology characterization and the XPS depth profiles of cycled LiMg-LiH@G. Top-view and cross-sectional SEM images of (**A** and **B**) bare Li and (**C** and **D**) LiMg-LiH@G electrodes after stripping and replating 2 mA hour cm^{-2} of Li, respectively, and (**E**) top-view and cross-sectional SEM images of the LiMg-LiH@G electrode after 100 cycles at 1 mA cm^{-2} for 1 mA hour cm^{-2}. (**F**) XPS depth profiles of the LiMg-LiH@G electrode after 20 cycles at 1 mA cm^{-2} for 1 mA hour cm^{-2}.

thus-formed full cells. The improved rate capability could be attributed to the fast ion/electron transfer of the LiMg-LiH@G electrode as proved by the lower polarization at high rates. Long-term cycling performance demonstrates that bare Li//LFP with a N/P ratio of ~5:1 (Fig. 4C and fig. S26) shows rapid capacity decay at 1 C after only 78 cycles, and only negligible capacity could be retained after 120 cycles due to the severe formation of Li dendrites and dead Li on the surface of Li metal anode with obvious cracks (Fig. 4D). SEM image validates that the thickness of the thus-formed porous and thick dead Li layer reaches ~30 μm for the bare Li anode, indicating that ~24% of the original bare Li electrode has been transformed to inactivated dead Li due to the large volume change during cycling, and hence the depletion of limited fresh Li underneath will eventually lead to rapid capacity fading. In sharp contrast, LiMg-LiH@G//LFP exhibits a stable cycling performance over 200 cycles with a capacity retention of 97.0% even with a lower N/P ratio of 4.2:1. The excellent cycling stability could be indirectly supported by the smooth and dense surface morphology and negligible thickness variation of the LiMg-LiH@G electrode after cycling (Fig. 4E). Moreover, full cells with ultrathin LiMg-LiH@G (50 μm, ~8.4 mA hour cm^{-2}) as the

anode and NCM523 (10 mg cm^{-2}, ~1.7 mA hour cm^{-2}) as the cathode are subsequently built for electrochemical performance investigation. Rate capability performance demonstrates that LiMg-LiH@G//NCM523 exhibits a higher reversible areal capacity of 1.57, 1.49, 1.40, 1.31, and 1.23 mA hour cm^{-2} at 0.2, 0.5, 1, 2, and 3 C, respectively, than that of the bare Li metal anode, especially at high rates (fig. S27). Moreover, induced by the uniform Li stripping and plating process (fig. S28), the LiMg-LiH@G//NCM523 full cell also delivers a high areal capacity of over 1.21 mA hour cm^{-2} after 215 cycles with a capacity retention of 79.1% at 1 C (fig. S29), while only a capacity of 0.29 mA hour cm^{-2} could be obtained for bare Li//NCM523 full cells after 68 cycles owing to the numerous formation of porous and thick dead Li. It is worth noting that the Li//NCM523 full cell is less stable than the Li//LFP full cell, which could be attributed to the poor stability of the NCM523 cathode (fig. S30) induced by residual species on the surface, microcracking of NCM particles, spontaneous side reactions, Li$^+$/Ni^{2+} mixing, and the dissolution of transition-metal ions (fig. S31). To further investigate the potential application of LiMg-LiH@G under practical conditions, the electrochemical performance of full cells with an ultrathin anode
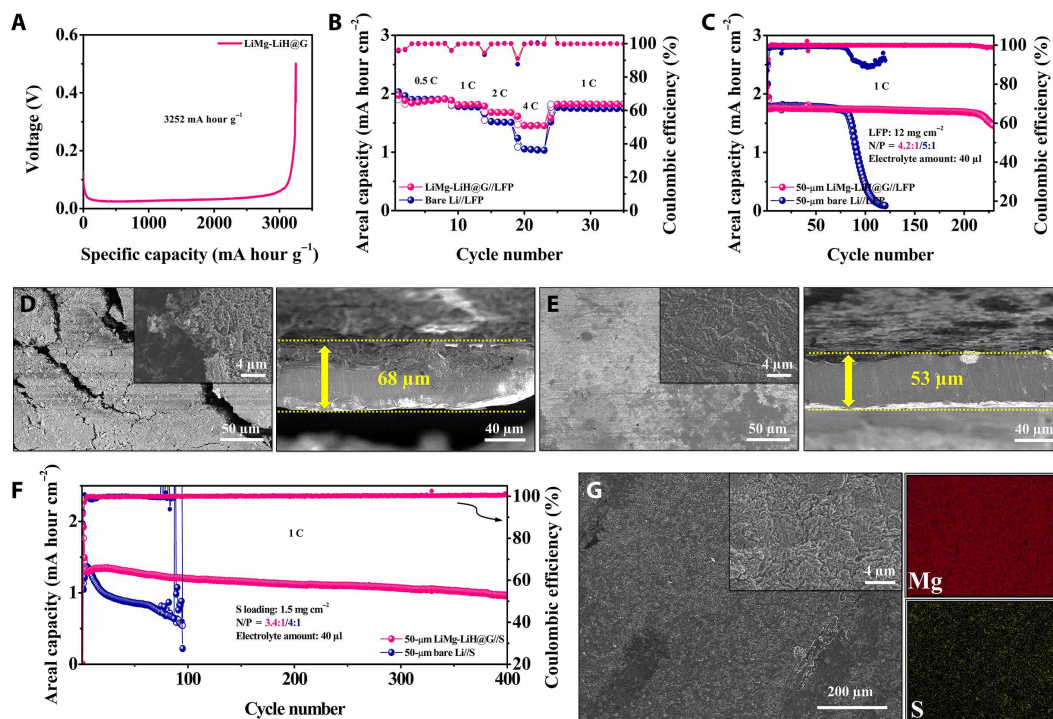
Fig. 4. Electrochemical performance of full cells and SEM characterization of cycled anodes. (**A**) Galvanostatic charge profile of LiMg-LiH@G. (**B**) Rate performance of LiMg-LiH@G//LFP and bare Li//LFP full cells at various rates from 0.5 C to 4 C (1 C = 170 mA g^{-1}). (**C**) Cycling performance of LiMg-LiH@G//LFP and bare Li//LFP full cells at 1 C. Top-view and cross-sectional SEM images of the (**D**) bare Li and (**E**) LiMg-LiH@G electrode taken from bare Li//LFP and LiMg-LiH@G//LFP after 50 cycles at 1 C, respectively. (**F**) Cycling performance of LiMg-LiH@G//S and bare Li//S full cells at 1 C (1 C = 1650 mA g^{-1}). (**G**) Top-view SEM image and the corresponding elemental mapping of the LiMg-LiH@G electrode taken from bare Li//S full cells after 50 cycles at 1 C.

and a high mass loading of an LFP cathode (LFP, 5 mA hour cm^{-2}) is further investigated. Upon cycling at 0.5 C (fig. S32), bare Li//LFP full cells show rapid capacity decay after only 40 cycles. In strong contrast, LiMg-LiH@G//LFP full cells exhibit a stable cycling performance of over 120 cycles with a capacity retention of 91.5% and stable voltage profiles. The improved cycling stability could be attributed to the favorable and uniform deposition/stripping of Li as observed in the LiMg-LiH@G.

The LiMg-LiH@G electrode is further used as the anode to couple with the Li-free S cathode (S loading, 1.5 mg cm^{-2}) for assembling Li-S full cells with a N/P ratio of 3.4 for the LiMg-LiH@G anode and 4.0 for the bare Li anode, respectively. Upon cycling at 1 C (1 C = 1650 mA g^{-1}), the areal capacity of bare Li//S rapidly drops to 0.6 mA hour cm^{-2} after only 90 cycles (Fig. 4F) owing to the rapid consumption of active Li due to the reaction between electrolyte and fresh Li and the formation of a porous dead Li layer (fig. S33A). Besides, as evidenced by the strong concentration of S element on the surface of the bare Li anode (fig. S34), the aggravated consumption of limited S and Li sources could also be observed on the surface of the bare Li anode after cycling due to the reaction of Li metal with soluble polysulfides resulting from the shuttle effect. In strong contrast, LiMg-LiH@G//S displays a much higher capacity of 0.97 mA hour cm^{-2} even after 400 cycles, with a capacity retention of 74.5% due to the uniform Li stripping and plating process of the LiMg-LiH@G electrode (fig. S33B). A lower content of S element could be observed on the surface of the LiMg-LiH@G electrode compared with the bare Li metal anode (Fig. 4G and fig. S35), suggesting the suppression of the reaction between polysulfides and Li.

To identify the positive role of LiMg-LiH@G in suppressing the corrosion of Li metal by polysulfides, the surface components are measured via in-depth XPS spectra (fig. S36). After 50 cycles, only one peak at 1303.5 eV could be observed in the Mg 1s spectrum of the LiMg-LiH@G electrode, which could be indexed to MgS/MgO (26). After Ar ion etching for 50 nm, the characteristic peak of LiMg alloys at 1302.5 eV appears to be accompanied by the significant decrease of the density of MgS/MgO signals. Moreover, the significant decrease of the intensity of Li$_2$S/MgS peaks could also be observed in Li 1s and S 2p spectra upon the proceeding of etching, indicating that Li$_2$S mainly forms on the surface of LiMg-LiH@G with the protection of LiMg alloys. It demonstrates that the erosion of anode could be effectively suppressed by building LiMg-LiH@G electrodes, leading to the prolonged life span of LiMg-LiH@G//S full cell. The intensity of Li$_2$S peaks on the bare Li metal anode, however, almost remains unchanged under identical conditions, indicating the severe corrosion of bare Li by polysulfides (fig. S37).

DISCUSSION
In summary, we have systematically investigated the role of LiH in stabilizing the Li stripping and plating process of LiMg alloys by building a unique 3D structured Li metal anode. Owing to the poor electronegativity of H in the ionic compound of LiH, the interfaces between LiH with high Li ion conductivity and LiMg alloys results in the formation of numerous stable built-in electric fields, which effectively boosts Li diffusion kinetics from the surface of LiH to the surface of LiMg alloys toward favorable Li plating into LiMg alloys.

Therefore, the diffusion coefficient of Li ions of the thus-obtained 3D structured Li metal anode composed of LiMg alloys confined into graphene-supported LiH nanoparticles is almost 10 times higher than that of pure LiMg alloys confined into graphene. In addition, the lithiophilic LiMg alloys are capable of acting as homogeneous nucleation sites, which synergistically contribute to stabilizing the Li stripping and plating process based on the reversible solid solution–based alloying reaction. Coupled with the important role of graphene frameworks in reducing local current density and alleviating the large volume change during the Li stripping and plating process, the as-fabricated LiMg-LiH@G with a high specific capacity of 3252 mA hour g^{-1} exhibits a long cycle life of over 1200 hours at 3 mA cm^{-2} with a fixed capacity of 5 mA hour cm^{-2}. Moreover, upon coupling the ultrathin LiMg-LiH@G foil (50 μm, ~8.4 mA hour cm^{-2}) as the anode with commercial LFP (12 mg cm^{-2}) and NCM523 (10 mg cm^{-2}) cathode, the assembled full cells show remarkable cycling stability of over 200 cycles at 1 C. This study provides a promising strategy to develop dendrite-free Li metal anodes with high energy density by adopting the unique role of LiH in stabilizing the Li stripping and plating process.

MATERIALS AND METHODS
All samples containing MgH$_2$@G, Mg@G, and Li metal were prepared in an argon-purified glove box (MBraun Labmaster) with moisture and oxygen levels below 0.1 parts per million.

Preparation of MgH$_2$@G and Mg@G
Graphene-confined MgH$_2$ nanoparticles were prepared via our previous work. Typically, 1.6 ml of dibutyl-magnesium solution (Sigma-Aldrich, 1 M in heptane), 13.6 mg of graphene, and 40 ml of cyclohexane (Sigma-Aldrich, 99.5%) were mixed in a pressure reactor vessel under vigorous stirring and ultrasonic treatment. Subsequently, the mixture was heated at 200°C under a hydrogen pressure of 4.5 MPa for 24 hours. After consecutive washing and centrifugation, the composites were dried under dynamic vacuum at 80°C for 12 hours on a Schlenk line to obtain MgH$_2$@G. The as-prepared MgH$_2$@G was dehydrogenated to obtain Mg@G.

Preparation of LiMg-LiH@G and LiMg-G
A certain amount of MgH$_2$@G/Mg@G was dispersed uniformly on Li foil and then rolled and pressed multiple times. MgH$_2$@G/Mg@G shows a porous structure and large volume, which is comparable to the volume of Li foil (fig. S38). Therefore, to ensure the uniform dispersion of MgH$_2$@G/Mg@G inside the as-fabricated Li metal anodes, the amount of MgH$_2$@G/Mg@G each time was controlled to be approximately 1.5 mg when using 120 mg of Li foil. This means that the rolling and pressing times for the initial fabrication of MgH$_2$@G-Li and Mg@G-Li are 4, 8, 12, and 16 for 5, 9, 13, and 17% LiMg-LiH@G and LiMg-G, respectively. After the initial rolling and pressing process, the as-obtained MgH$_2$@G-Li and Mg@G-Li were heated at 280°C under vigorous stirring for 30 min to further promote the uniform distribution between LiMg alloys and LiH and graphene and avoid the possible aggregation of LiH and graphene. Moreover, the uniform distribution of LiH inside LiMg alloys could effectively avoid contamination of the as-prepared LiH. Subsequently, the LiMg-LiH@G and LiMg-G were rolled and pressed for about 20 times before cutting into 12-mm-diameter electrodes for symmetric and full-cell tests.

Materials characterization
The phase composition of as-prepared samples was measured by XRD (Bruker D8 Advance) with Cu Kα radiation (λ = 1.5418 Å). XPS (Thermo Fisher Scientific K-Alpha$^+$) experiments were performed with a single x-ray source, using an Al Kα (1486 eV) anode. The pressure in the analysis room during data acquisition was maintained at ≤2 × 10^{-7} mbar. All binding energies were calibrated by using the contaminant carbon (C 1s = 284.8 eV) as a reference. The morphology of as-prepared samples was determined with a scanning electron microscope (SEM, FEI Nova Nano 450) and a transmission electron microscope (JEOL 2011F).

Electrochemical measurement
The electrochemical performance was tested in CR2032-type coin cells with a Celgard 2500 separator. LiTFSI (1 M) in 1,3-dioxolane and dimethoxyethane (1:1 in volume) with 0.2 M LiNO$_3$ was used as an electrolyte of symmetric and Li//S cells. Lithium hexafluorophosphate (1 M) in ethylene carbonate and diethyl carbonate (1/1 in volume) with the addition of 10 wt % fluoroethylene carbonate and 1% vinylene carbonate was used as an electrolyte of symmetric, Li//LFP, and Li//NCM523 cells. The volume of electrolyte in each cell was 40 μl. In symmetric cells, Li metal electrodes (12 mm in diameter) were used as both working and counter electrodes. In Li//LFP and Li//NCM523 full cells, LFP and NCM523 cathodes were purchased from Canrd (Guangdong Canrd New Energy Technology Co. Ltd). The active mass loading of LFP and NCM523 was about 12 and 10 mg cm^{-2}, respectively. In Li//S full cells, the carbon-sulfur composite was first prepared by mixing CMK-3 and sublimated sulfur (4:6 in weight) and then heated at 155°C for 12 hours. Sulfur cathodes were then prepared by casting N-methyl-2-pyrrolidinone slurry containing carbon-sulfur composite (80 wt %), CNTs (10 wt %), and polyvinylidene fluoride (10 wt %) onto Al foil, followed by drying at 55°C under vacuum for 12 hours. The loading amount of S on sulfur cathodes is about 1.5 mg cm^{-2}. Before assembling full cells, Li metal electrodes (bare Li and LiMg-LiH@G) were rolled and pressed to obtain foils with a thickness of about 50 μm. All electrodes were punched into disks with a diameter of 12 mm.

The cycling performance of symmetric cells and full cells was carried out on a LAND battery testing system at room temperature. The voltage window for Li//LFP, Li//NCM523, and Li//S full cells was 2.5 to 4 V, 3 to 4.3 V, and 1.7 to 2.8 V, respectively. The EIS measurements were performed over a frequency range of 100 kHz to 100 mHz. Linear sweep voltammetry (LSV) was conducted at a fixed sweep rate of 1 mV s^{-1} with the voltage range from −200 to 200 mV. The corresponding exchange current density was calculated by linear fitting (from −150 to −100 mV). Both EIS and LSV measurements were conducted on a SP-300 electrochemical workstation (Bio-Logic). The Li$^+$ diffusion coefficient (D_{Li}) of MgH$_2$@G and Mg@G during lithiation was calculated using GITT based on Eq. 1, where n_m, V_m, and S are the molar number, molar volume, and electrode surface area of LiMg-LiH@G/LiMg-G, respectively; ΔE_s stands for the voltage variation during current pulse, and ΔE_t denotes the voltage drop during galvanostatic discharge of MgH$_2$@G/Mg@G

$$D_{Li} = \frac{4}{\pi\tau}\left(\frac{n_m V_m}{S}\right)^2 \left(\frac{\Delta E_s}{\Delta E_t}\right)^2 \tag{1}$$

Theoretical calculation

DFT calculations were carried out using the projector-augmented wave method as implemented in Vienna ab initio simulation package (*32–34*). A generalized gradient approximation of Perdew-Burke-Ernzerhof functional was used to describe the exchange-correlation interaction (*35*). An energy cutoff of 500 eV and Gamma-centered $3 \times 3 \times 1$ k-points mesh were applied to all calculations. Li_3Mg (001) and LiH (001) were selected to simulate the interfaces in the electrode. The vacuum layer of 20 Å was adopted in all calculations. The structures were relaxed until the forces and total energy on all atoms were converged to less than 0.05 eV Å^{-1} and 1×10^{-5} eV. To evaluate the interaction between Li and the electrode, the binding energy (E_b) was calculated as follows

$$E_b = E_{Total} - E_{Li} - E_{sub}$$

where E_{sub} and E_{Total} are the total energy of compound before and after Li deposition, respectively. E_{Li} is the energy of a single Li atom. The lower the binding energy, the stronger the interaction between Li and electrode. Activation barriers for deposited Li hopping between adjacent interstitial sites in the interfaces were calculated using the climbing-image nudged elastic band method (*36*).

SUPPLEMENTARY MATERIALS

Supplementary material for this article is available at https://science.org/doi/10.1126/sciadv.abl8245

REFERENCES AND NOTES

1. J. M. Tarascon, M. Armand, Issues and challenges facing rechargeable lithium batteries. *Nature* **414**, 359–367 (2001).
2. V. Etacheri, R. Marom, R. Elazari, G. Salitra, D. Aurbach, Challenges in the development of advanced Li-ion batteries: A review. *Energ. Environ. Sci.* **4**, 3243–3262 (2011).
3. P. Albertus, S. Babinec, S. Litzelman, A. Newman, Status and challenges in enabling the lithium metal electrode for high-energy and low-cost rechargeable batteries. *Nat. Energy* **3**, 16–21 (2018).
4. X.-B. Cheng, R. Zhang, C.-Z. Zhao, Q. Zhang, Toward safe lithium metal anode in rechargeable batteries: A review. *Chem. Rev.* **117**, 10403–10473 (2017).
5. D. Lin, Y. Liu, Y. Cui, Reviving the lithium metal anode for high-energy batteries. *Nat. Nanotechnol.* **12**, 194–206 (2017).
6. B. Li, Y. Wang, S. Yang, A material perspective of rechargeable metallic lithium anodes. *Adv. Energy Mater.* **8**, 1702296 (2018).
7. R. Bouchet, S. Maria, R. Meziane, A. Aboulaich, L. Lienafa, J.-P. Bonnet, T. N. T. Phan, D. Bertin, D. Gigmes, D. Devaux, R. Denoyel, M. Armand, Single-ion bab triblock copolymers as highly efficient electrolytes for lithium-metal batteries. *Nat. Mater.* **12**, 452–457 (2013).
8. F. Ding, W. Xu, G. L. Graff, J. Zhang, M. L. Sushko, X. Chen, Y. Shao, M. H. Engelhard, Z. Nie, J. Xiao, X. Liu, P. V. Sushko, J. Liu, J.-G. Zhang, Dendrite-free lithium deposition via self-healing electrostatic shield mechanism. *J. Am. Chem. Soc.* **135**, 4450–4456 (2013).
9. R. Bhattacharyya, B. Key, H. Chen, A. S. Best, A. F. Hollenkamp, C. P. Grey, In situ NMR observation of the formation of metallic lithium microstructures in lithium batteries. *Nat. Mater.* **9**, 504–510 (2010).
10. D. Lu, Y. Shao, T. Lozano, W. D. Bennett, G. L. Graff, B. Polzin, J. Zhang, M. H. Engelhard, N. T. Saenz, W. A. Henderson, P. Bhattacharya, J. Liu, J. Xiao, Failure mechanism for fast-charged lithium metal batteries with liquid electrolytes. *Adv. Energy Mater.* **5**, 1400993 (2015).
11. Z. Shadike, H. Lee, O. Borodin, X. Cao, X. Fan, X. Wang, R. Lin, S.-M. Bak, S. Ghose, K. Xu, C. Wang, J. Liu, J. Xiao, X.-Q. Yang, E. Hu, Identification of LiH and nanocrystalline LiF in the solid–electrolyte interphase of lithium metal anodes. *Nat. Nanotechnol.* **16**, 549–554 (2021).
12. M. J. Zachman, Z. Tu, S. Choudhury, L. A. Archer, L. F. Kourkoutis, Cryo-STEM mapping of solid–liquid interfaces and dendrites in lithium-metal batteries. *Nature* **560**, 345–349 (2018).
13. G. Xu, J. Li, C. Wang, X. Du, D. Lu, B. Xie, X. Wang, C. Lu, H. Liu, S. Dong, G. Cui, L. Chen, The formation/decomposition equilibrium of LiH and its contribution on anode failure in practical lithium metal batteries. *Angew. Chem. Int. Ed.* **60**, 7770–7776 (2021).
14. H. Zhang, U. Oteo, X. Judez, G. G. Eshetu, M. Martinez-Ibañez, J. Carrasco, C. Li, M. Armand, Designer anion enabling solid-state lithium-sulfur batteries. *Joule* **3**, 1689–1702 (2019).
15. M. Wan, S. Kang, L. Wang, H.-W. Lee, G. W. Zheng, Y. Cui, Y. Sun, Mechanical rolling formation of interpenetrated lithium metal/lithium tin alloy foil for ultrahigh-rate battery anode. *Nat. Commun.* **11**, 829 (2020).
16. H. S. Wang, D. C. Lin, Y. Y. Liu, Y. Z. Li, Y. Cui, Ultrahigh–current density anodes with interconnected Li metal reservoir through overlithiation of mesoporous AlF$_3$ framework. *Sci. Adv.* **3**, e1701301 (2017).
17. S. Liu, Y. Ma, Z. Zhou, S. Lou, H. Huo, P. Zuo, J. Wang, C. Du, G. Yin, Y. Gao, Inducing uniform lithium nucleation by integrated lithium-rich Li-In anode with lithiophilic 3D framework. *Energy Storage Mater.* **33**, 423–431 (2020).
18. X.-Y. Yue, W.-W. Wang, Q.-C. Wang, J.-K. Meng, Z.-Q. Zhang, X.-J. Wu, X.-Q. Yang, Y.-N. Zhou, CoO nanofiber decorated nickel foams as lithium dendrite suppressing host skeletons for high energy lithium metal batteries. *Energy Storage Mater.* **14**, 335–344 (2018).
19. X.-Y. Yue, W.-W. Wang, Q.-C. Wang, J.-K. Meng, X.-X. Wang, Y. Song, Z.-W. Fu, X.-J. Wu, Y.-N. Zhou, Cuprite-coated Cu foam skeleton host enabling lateral growth of lithium dendrites for advanced Li metal batteries. *Energy Storage Mater.* **21**, 180–189 (2019).
20. G. Xia, Y. Tan, X. Chen, D. Sun, Z. Guo, H. Liu, L. Ouyang, M. Zhu, X. Yu, Monodisperse magnesium hydride nanoparticles uniformly self-assembled on graphene. *Adv. Mater.* **27**, 5981–5988 (2015).
21. H. Zhang, S. Ju, G. Xia, D. Sun, X. Yu, Dendrite-free Li-metal anode enabled by dendritic structure. *Adv. Funct. Mater.* **31**, 2009712 (2021).
22. T. Ma, T.-Y. Su, L. Zhang, J.-W. Yang, H.-B. Yao, L.-L. Lu, Y.-F. Liu, C. He, S.-H. Yu, Scallion-inspired graphene scaffold enabled high rate lithium metal battery. *Nano Lett.* **21**, 2347–2355 (2021).
23. T. Yang, L. Li, F. Wu, R. Chen, A soft lithiophilic graphene aerogel for stable lithium metal anode. *Adv. Funct. Mater.* **30**, 2002013 (2020).
24. D. Lin, Y. Liu, Z. Liang, H.-W. Lee, J. Sun, H. Wang, K. Yan, J. Xie, Y. Cui, Layered reduced graphene oxide with nanoscale interlayer gaps as a stable host for lithium metal anodes. *Nat. Nanotechnol.* **11**, 626–632 (2016).
25. S. Jin, Y. Ye, Y. Niu, Y. Xu, H. Jin, J. Wang, Z. Sun, A. Cao, X. Wu, Y. Luo, H. Ji, L.-J. Wan, Solid–solution-based metal alloy phase for highly reversible lithium metal anode. *J. Am. Chem. Soc.* **142**, 8818–8826 (2020).
26. L.-L. Kong, L. Wang, Z.-C. Ni, S. Liu, G.-R. Li, X.-P. Gao, Lithium–magnesium alloy as a stable anode for lithium–sulfur battery. *Adv. Funct. Mater.* **29**, 1808756 (2019).
27. Y. Deng, M. Wang, C. Fan, C. Luo, Y. Gao, C. Zhou, J. Gao, Strategy to enhance the cycling stability of the metallic lithium anode in Li-metal batteries. *Nano Lett.* **21**, 1896–1901 (2021).
28. H. Qiu, T. Tang, M. Asif, W. Li, T. Zhang, Y. Hou, Stable lithium metal anode enabled by lithium metal partial alloying. *Nano Energy* **65**, 103989 (2019).
29. S.-S. Chi, Y. Liu, W.-L. Song, L.-Z. Fan, Q. Zhang, Prestoring lithium into stable 3D nickel foam host as dendrite-free lithium metal anode. *Adv. Funct. Mater.* **27**, 1700348 (2017).
30. D. Luo, L. Zheng, Z. Zhang, M. Li, Z. Chen, R. Cui, Y. Shen, G. Li, R. Feng, S. Zhang, G. Jiang, L. Chen, A. Yu, X. Wang, Constructing multifunctional solid electrolyte interface via in-situ polymerization for dendrite-free and low N/P ratio lithium metal batteries. *Nat. Commun.* **12**, 186 (2021).
31. X. Wang, S. Li, W. Zhang, D. Wang, Z. Shen, J. Zheng, H. L. Zhuang, Y. He, Y. Lu, Dual-salt-additive electrolyte enables high-voltage lithium metal full batteries capable of fast-charging ability. *Nano Energy* **89**, 106353 (2021).
32. G. Kresse, J. Furthmüller, Efficient iterative schemes for ab initio total-energy calculations using a plane-wave basis set. *Phys. Rev. B* **54**, 11169–11186 (1996).
33. G. Kresse, Ab initio molecular dynamics for liquid metals. *J. Non Cryst. Solids* **192–193**, 222–229 (1995).
34. P. E. Blöchl, Projector augmented-wave method. *Phys. Rev. B* **50**, 17953–17979 (1994).
35. J. P. Perdew, K. Burke, M. Ernzerhof, Generalized gradient approximation made simple. *Phys. Rev. Lett.* **77**, 3865–3868 (1996).
36. G. Henkelman, H. Jónsson, Improved tangent estimate in the nudged elastic band method for finding minimum energy paths and saddle points. *J. Chem. Phys.* **113**, 9978–9985 (2000).
37. C.-P. Yang, Y.-X. Yin, S.-F. Zhang, N.-W. Li, Y.-G. Guo, Accommodating lithium into 3D current collectors with a submicron skeleton towards long-life lithium metal anodes. *Nat. Commun.* **6**, 8058 (2015).
38. S. Liu, L. Deng, W. Guo, C. Zhang, X. Liu, J. Luo, Bulk nanostructured materials design for fracture-resistant lithium metal anodes. *Adv. Mater.* **31**, 1807585 (2019).
39. R. Zhang, X. Chen, X. Shen, X.-Q. Zhang, X.-R. Chen, X.-B. Cheng, C. Yan, C.-Z. Zhao, Q. Zhang, Coralloid carbon fiber-based composite lithium anode for robust lithium metal batteries. *Joule* **2**, 764–777 (2018).
40. P. Zou, Y. Wang, S.-W. Chiang, X. Wang, F. Kang, C. Yang, Directing lateral growth of lithium dendrites in micro-compartmented anode arrays for safe lithium metal batteries. *Nat. Commun.* **9**, 464 (2018).
41. M. S. Kim, Deepika, S. H. Lee, M.-S. Kim, J.-H. Ryu, K.-R. Lee, L. A. Archer, W. I. Cho, Enabling reversible redox reactions in electrochemical cells using protected LiAl intermetallics as lithium metal anodes. *Sci. Adv.* **5**, eaax5587 (2019).

42. B. Li, D. Zhang, Y. Liu, Y. Yu, S. Li, S. Yang, Flexible Ti$_3$C$_2$ MXene-lithium film with lamellar structure for ultrastable metallic lithium anodes. *Nano Energy* **39**, 654–661 (2017).

43. L. Liu, Y.-X. Yin, J.-Y. Li, N.-W. Li, X.-X. Zeng, H. Ye, Y.-G. Guo, L.-J. Wan, Free-standing hollow carbon fibers as high-capacity containers for stable lithium metal anodes. *Joule* **1**, 563–575 (2017).

44. S. Liu, X. Ji, J. Yue, S. Hou, P. Wang, C. Cui, J. Chen, B. Shao, J. Li, F. Han, J. Tu, C. Wang, High interfacial-energy interphase promoting safe lithium metal batteries. *J. Am. Chem. Soc.* **142**, 2438–2447 (2020).

45. Y. Zhang, W. Luo, C. Wang, Y. Li, C. Chen, J. Song, J. Dai, E. M. Hitz, S. Xu, C. Yang, Y. Wang, L. Hu, High-capacity, low-tortuosity, and channel-guided lithium metal anode. *Proc. Natl. Acad. Sci. U.S.A.* **114**, 3584–3589 (2017).

46. S. Liu, X. Xia, S. Deng, L. Zhang, Y. Li, J. Wu, X. Wang, J. Tu, Large-scale synthesis of high-quality lithium-graphite hybrid anodes for mass-controllable and cycling-stable lithium metal batteries. *Energy Storage Mater.* **15**, 31–36 (2018).

47. P. Shi, T. Li, R. Zhang, X. Shen, X.-B. Cheng, R. Xu, J.-Q. Huang, X.-R. Chen, H. Liu, Q. Zhang, Lithiophilic LiC$_6$ layers on carbon hosts enabling stable Li metal anode in working batteries. *Adv. Mater.* **31**, 1807131 (2019).

48. S. Wu, T. Jiao, S. Yang, B. Liu, W. Zhang, K. Zhang, Lithiophilicity conversion of the Cu surface through facile thermal oxidation: Boosting a stable Li–Cu composite anode through melt infusion. *J. Mater. Chem. A* **7**, 5726–5732 (2019).

49. Y. Liu, D. Lin, Z. Liang, J. Zhao, K. Yan, Y. Cui, Lithium-coated polymeric matrix as a minimum volume-change and dendrite-free lithium metal anode. *Nat. Commun.* **7**, 10992 (2016).

50. W. Go, M.-H. Kim, J. Park, C. H. Lim, S. H. Joo, Y. Kim, H.-W. Lee, Nanocrevasse-rich carbon fibers for stable lithium and sodium metal anodes. *Nano Lett.* **19**, 1504–1511 (2019).

51. F. Liu, R. Xu, Z. Hu, S. Ye, S. Zeng, Y. Yao, S. Li, Y. Yu, Regulating lithium nucleation via cnts modifying carbon cloth film for stable Li metal anode. *Small* **15**, 1803734 (2019).

52. C.-Y. Wang, Z.-J. Zheng, Y.-Q. Feng, H. Ye, F.-F. Cao, Z.-P. Guo, Topological design of ultrastrong mxene paper hosted Li enables ultrathin and fully flexible lithium metal batteries. *Nano Energy* **74**, 104817 (2020).

53. X.-Y. Yue, X.-L. Li, W.-W. Wang, D. Chen, Q.-Q. Qiu, Q.-C. Wang, X.-J. Wu, Z.-W. Fu, Z. Shadike, X.-Q. Yang, Y.-N. Zhou, Wettable carbon felt framework for high loading Li-metal composite anode. *Nano Energy* **60**, 257–266 (2019).

54. X.-R. Chen, B.-Q. Li, C. Zhu, R. Zhang, X.-B. Cheng, J.-Q. Huang, Q. Zhang, A coaxial-interweaved hybrid lithium metal anode for long-lifespan lithium metal batteries. *Adv. Energy Mater.* **9**, 1901932 (2019).

55. Y. Zhou, X. Zhang, Y. Ding, L. Zhang, G. Yu, Reversible deposition of lithium particles enabled by ultraconformal and stretchable graphene film for lithium metal batteries. *Adv. Mater.* **32**, 2005763 (2020).

56. J. Qian, S. Wang, Y. Li, M. Zhang, F. Wang, Y. Zhao, Q. Sun, L. Li, F. Wu, R. Chen, Lithium induced nano-sized copper with exposed lithiophilic surfaces to achieve dense lithium deposition for lithium metal anode. *Adv. Funct. Mater.* **31**, 2006950 (2021).